



Original paper

Simultaneous attenuation and scatter correction of PET data in the image: quantitative and clinical assessment of image-to-image deep learning models

Avishan Elkayee Dehno^{a,b}, Pardis Ghafarian^{c,d}, Hossein Arabi^e , Mohammad Reza Ay^{a,b,*}

^a Department of Medical Physics and Biomedical Engineering, Tehran University of Medical Sciences, Tehran, Iran

^b Research Center for Molecular and Cellular Imaging (RCMCI), Advanced Medical Technologies and Equipment Institute (AMTEI), Tehran University of Medical Sciences, Tehran, Iran

^c Chronic Respiratory Diseases Research Center, National Research Institute of Tuberculosis and Lung Diseases (NRITLD), Shahid Beheshti University of Medical Sciences, Tehran, Iran

^d PET/CT and Cyclotron Center, Masih Daneshvari Hospital, Shahid Beheshti University of Medical Sciences, Tehran, Iran

^e Division of Nuclear Medicine and Molecular Imaging, Geneva University Hospital, CH-1211 Geneva, Switzerland

ARTICLE INFO

Keywords:

PET-CT
Brain imaging
Attenuation and scatter correction
Deep learning
Radiomic features
GAN
UNET

ABSTRACT

Background: Positron Emission Tomography (PET) non-invasively assesses body metabolism but requires correction for photon attenuation and scatter.

Purpose: This study aims to convert non-attenuation scatter corrected (NASC) brain PET/CT images to measured attenuation and scatter corrected (MASC) images using deep learning algorithms.

Methods: In this study, brain PET/CT (¹⁸F-FDG) images of 125 patients diagnosed with epilepsy disorder were used. Two convolutional neural networks, UNET and CGAN, were implemented to take 2D-NASC inputs and generate MASC images. For a precise evaluation, segmentation of 83 brain regions and the calculation of 19 radiomic features for each region were performed, and paired sample *t*-test was conducted for each region to determine significant differences between the predicted and ground-truth images. Clinical evaluation was performed by nuclear medicine physicians.

Results: The mean Peak Signal-to-Noise Ratio (PSNR), Structural Similarity Index Measure (SSIM), and Root Mean Square Error (RMSE) were 41.55 ± 3.55 (dB), 0.997 ± 0.002 , and 294.8 ± 131.0 (Bq/ml) for the CGAN model, and 40.70 ± 3.84 (dB), 0.996 ± 0.003 , and 327.6 ± 163.8 (Bq/ml) for the UNET model, respectively. Among 1,577 paired values of radiomic features in different brain regions of test set, only 126 (CGAN) and 156 (UNET) values showed significant differences from the corresponding MASC values, indicating that the majority of radiomic features were well preserved while still highlighting subtle textural variations. In clinical evaluation, the UNET and CGAN models demonstrated strong performance in visual quality assessment.

Conclusion: Direct attenuation and scatter correction using both convolutional deep networks is a promising approach for brain PET images, when CT is not available.

1. Introduction

Positron Emission Tomography (PET) is a 3D non-invasive imaging modality that can be used to demonstrate metabolic and functional information of brain, such as neurotransmitters activity, which is used for diagnosis and localization of abnormalities [1]. The ¹⁸F-FDG is the most frequently used radiotracer in PET scans for diagnostic purposes, particularly in the early stages before the manifestation of structural

alternations or clinical symptoms [2].

Brain PET images offer valuable quantitative and semi-quantitative metrics which provide essential information from physiological processes. In order to achieve precise and accurate quantitative analysis and suitable qualitative interpretation, it is imperative to apply some critical post-acquisition corrections on PET images [3]. Attenuation and scatter are two tissue-dependent phenomena [4], which both occur because of the inherent properties of photons due to photoelectric and Compton

* Corresponding author at: Department of Medical Physics and Biomedical Engineering, Tehran University of Medical Sciences, Tehran, Iran.

E-mail address: Mohammadreza.ay@tums.ac.ir (M.R. Ay).

<https://doi.org/10.1016/j.ejmp.2025.105683>

Received 8 June 2025; Received in revised form 16 September 2025; Accepted 28 November 2025

Available online 6 December 2025

1120-1797/© 2025 Associazione Italiana di Fisica Medica e Sanitaria. Published by Elsevier Ltd. All rights are reserved, including those for text and data mining, AI training, and similar technologies.

events [4,5]. These events may lead to decrease or increase number of detected counts within certain regions, can result in underestimation or overestimation of the radiotracer uptake [6].

In hybrid PET/CT imaging, the attenuation correction (AC) method involves computing attenuation factors from the attenuation map obtained from the CT scan [7]. However, incorporating this additional anatomic image increases ionizing radiation to the patient [8], which is crucial especially in patients requiring repetitive PET/CT, considering their long-term health implications [9]. In certain situations, CT-based attenuation correction can be unreliable, including motion-degraded [10,11] or artifact-affected [12] CT scans. Moreover, challenges occur on AC in PET/MRI [13–15] and dedicated brain PET scanners [16,17] while the CT attenuation map is not available. Although MR-based attenuation correction has advanced over the years with techniques such as, HUGE [18], UTE/ZTE [19,20], and SEGBONE [21], as well as emission-based [22] and atlas-based [23] methods. These techniques use MR images to generate attenuation maps, while CT-based attenuation correction remains more accurate, particularly in cortical and bone regions [24].

Dedicated brain PET systems have been widely developed in recent years, aimed at improving accessibility, resolution, and patient comfort. Examples include the NeuroLF [25] an ultra-compact device for diagnosing brain disorders including epilepsy, Alzheimer's, and brain tumors, PhotoDiagnostics [26] a mobile and flexible human and animal brain PET with good quality, resolution, sensitivity and count rate performance and the HIAS-29000 [27], a high-resolution dedicated brain PET system developed to improve sensitivity and spatial resolution. These developments highlight the growing interest in specialized neuroimaging devices, emphasizing the need for attenuation and scatter correction where CT data are not available.

On a separate procedure from AC, several scatter correction (SC) approaches exist that can be applied in hybrid PET/CT scanners, while the gold standard method, Monte Carlo, faces limitations due to its complex computational requirements [28]. Due to common issues with CT-based attenuation correction, lack of access to CT images in devices such as PET/MRI and dedicated brain PET [16,17] and complication of analytical scatter correction, deep learning networks have been proposed as an alternative method.

Deep learning (DL) has been widely applied on medical images analysis, as it can extract intricate information from images which are not able to be extracted manually [29,30]. DL algorithms have been expanded in various image analysis applications, including resolution recovery [1,31], denoising [32], segmentation [33,34], reconstruction [35], super-resolution [36], synthesis of images [37]. Image-to-image translation is one of the techniques of DL that aims to convert input image from one domain into a corresponding output image in another domain. Two of the most commonly used algorithms in image-to-image translation are UNET [30] and Generative Adversarial Networks (GANs) [38], which have been widely used to generate medical images in one modality using images from another [39], such as converting PET to CT [8,40], MRI to CT [41,42], and non-attenuation scatter corrected (NASC) PET to measured attenuation scatter corrected (MASC) PET [2,43,44].

Various architectural configurations applied across different domains (image and sinogram) for the task of attenuation and scatter correction in PET imaging [45,46]. One approach is generating pseudo-CT, from non-corrected PET or MR images, which the evaluation contains comparing real and pseudo-CT, and PET images corrected by reference and synthetic CT images [47]. For instance, Armanious et al. [40] used CGAN model to generate CT from non-attenuation corrected PET on brain images. The results from both studies demonstrated a strong visual resemblance, with an SUV difference of less than 5 % in brain regions [40,48]. Moreover Arabi et al. [41] implemented DL-AdvSS to convert T1-weighted MR images to pseudo-CT. These methods will further use pseudo-CT to generate attenuation maps for PET images. The DL-AdvSS and atlas technique presented comparable

performance in estimating CT values in cortical bone region, and mean SUV bias below 4 % across 63 brain regions [41]. Another approach is direct generation of corrected PET from non-corrected input images, as Yang et al. [2] used deep convolutional neural networks (DCNN), a one-step-process, for joint attenuation and scatter correction (ASC) on PET images. The mean SUV difference of -0.8 ± 5.2 % suggests the potential for this method to be considered as an alternative to MR-ASC in PET/MRI applications [2].

The UNET algorithm is a derivative of Deep Convolutional Neural Network (DCNN) algorithm, well-known for its efficacy on image-to-image translation tasks [33]. On the other hand, GAN models contain adversarial training through generator and discriminator networks, which compete, generator to fabricate fake data and discriminator to accurately distinguish real and synthetic instances [49]. The innovation on GAN models extends to algorithms such as Conditional GAN (CGAN), which incorporates additional information to guide the generator. A specialized derivation of the CGAN framework is the image-to-image translation domain, where pairs of corresponding images enable the transformation between image modalities [50]. Utilizing these algorithms in ASC efficiently minimizes patient dose exposure and reduces errors that could potentially occur with traditional methods [51].

In this study, UNET and CGAN were implemented to apply simultaneous ASC on brain PET images without the prerequisite of anatomical imaging modalities such as CT scans (direct application of the attenuation and scatter correction in the image domain). NASC images were fed into these models to generate MASC scans.

2. Material and methods

2.1. Patient data

Total 125 brain PET/CT scans were retrospectively acquired from patients who had epilepsy disorders. Patients were fasting for 6 h prior to radiopharmaceutical administration, with blood glucose level below 150 mg/dL (8.3 mmol/L), ^{18}F -FDG administration of 4.5 MBq/Kg. Imaging data were acquired using GE Discovery 690 PET/CT scanner after an uptake of 60 ± 7 -minutes. Half of the PET images were acquired using the time-of-flight and PSF technique and the others only with PSF. CT data collection performed via GE VCT64 slice of GE discovery 690 PET/CT scanner, under same circumstances and similar parameters considered, including pitch factor (0.98:1), smart tube current, voltage (120 kVp), gantry rotation time (1 –s). PET-data were gathered on 256×256 matrix size with $1.9531 \times 1.9531 \times 3.27$ mm³ voxel dimension, while CT-data acquired on 512×512 matrix and voxel size of $0.9766 \times 0.9766 \times 3.27$ mm³. Reconstruction algorithm applied on PET data using ordered subset expectation maximization (OSEM) with 2 and 3 iterations, 24 subsets, and a Gaussian post-smoothing filter with 4 –mm FWHM. Both NASC and MASC images were reconstructed using the same parameters and standard corrections (e.g., randoms, decay, and normalization). The only difference was in attenuation and scatter correction: NASC images were reconstructed without either correction, whereas MASC images included both.

The retrospective dataset was acquired between 2017 and 2024, with the first years collected without TOF capability and reconstructed with PSF only, and subsequent scans acquired after the implementation of TOF and reconstructed with TOF + PSF. In an earlier study [52], we compared three training regimes—TOF-only, PSF-only, and a mixed regime including both types—while keeping the total number of training samples constant and evaluating performance on the same independent test set. A preliminary analysis indicated that, keeping constant total sample size, training on a mixed set of TOF + PSF and PSF-only scans improved prediction accuracy compared to training on TOF + PSF or PSF-only data. Therefore, the dataset used in this study included two reconstruction types: TOF + PSF and PSF-only.

The dataset has been divided into train (113patients) and test (12patients) groups, including 90 % and 10 % of the total sample size,

respectively. The training set contains 57 female and 56 male patients, with an average age of 38.8 ± 17.8 years. In the test group, there are 6 patients of each gender, total of 12 patients, with an average age of 39 ± 20.1 years. The mean weight of patients in the training and test groups is 72.92 ± 17.94 kg and 74.8 ± 15.69 kg, respectively. To enhance model performance, pixel values have been normalized within the range of 0 to 1. Moreover, standard image augmentation techniques (rotation (10°), horizontal and vertical translations (0.1), shearing (0.1), and zooming (0.1)) were applied randomly on training dataset to double the number of data and counter overfitting. These images also help the models to become generalizable to these variations on images.

3. Deep learning models

3.1. UNET

The designed UNET model takes NASC brain PET images as input and generates the corresponding MASC images. This translation is achieved by extracting features from input on encoding path. Subsequently, the high-resolution output is reconstructed on the almost symmetric decoding path. To enhance the restoration of spatial details, skip connections were employed [33]. We applied transfer learning, by using the pre-trained VGG16 model weights trained on ImageNet dataset as the encoder [53]. The output layer of the model is a 1×1 convolutional layer with a sigmoid activation function and result in generating MASC images (Fig. 1).

3.2. CGAN

Additionally, CGAN model has been designed, which creates new data instances through generator model, and later the discriminator model aims to distinguish between real and generated (fake) data. Both networks are trained competitively and help each other to achieve superior performance. Previously described UNET model has been used as generator in CGAN, which receives NASC as input and produce DL-MASC. In next step NASC and MASC will be concatenated and create a merged input tensor, which enters to a convolutional "PatchGAN" classifier discriminator [50] (Fig. 2).

4. Models implementation

4.1. UNET

The proposed UNET model is compiled using the Mean Squared Error (MSE (Equation S1)) loss function, which quantifies the difference between MASC (ground-truth) and DL-MASC (prediction). The model is optimized using the Adam (Adaptive Moment Estimation) with 0.001 learning rate. The training was performed with 1000 epochs and mini-batch of 47 (number of slices for each patient); although only after 50 epochs it reached convergence (Fig. S1). During the training process, 10 % of dataset was dedicated to validation set.

4.2. CGAN

CGAN implementation involves alternative training of generator and discriminator. The adversarial training procedure between generator and discriminator will be guided through adversarial loss, which is Binary-Cross-Entropy (BCE) loss function. Total loss for generator is the weighted sum of adversarial loss (BCE) and L-1 loss (MAE) which the later one calculates difference between MASC and DL-MASC. The training process with Adam optimizer, a learning rate of 0.001, iterates for 100 epochs, and 1,062,200 steps with mini-batch = 1, and the trained model has been saved every 10 epochs. Unlike the UNET training, no external validation set was used and periodic checkpoints served as interim validation to monitor performance. When the generator is well-trained and produces realistic data from NASC input, the discriminator can no longer distinguish it from real samples.

5. Assessment strategy

Quantifying the quality of DL-MASC images in test set compared to corresponding MASC, applied using various metrics such as root mean squared error (RMSE (Equation S2)), peak signal-to-noise ratio (PSNR (Equation S3)), and structural similarity index metrics (SSIM (Equation S4)). The average values of these metrics have been calculated separately for TOF + PSF and PSF reconstructed data and mixed (both TOF + PSF and PSF groups) patients in test set. Since former metrics applied

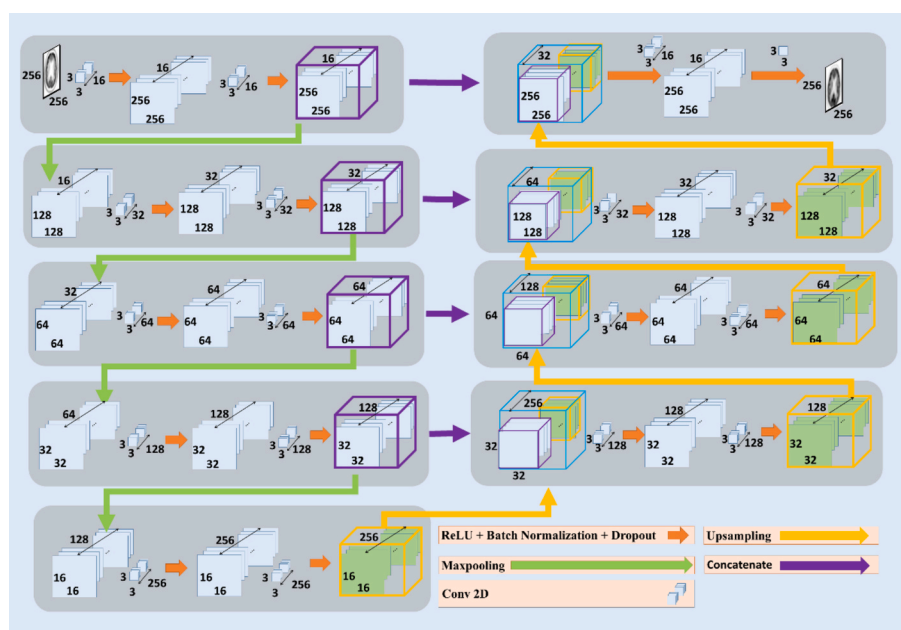


Fig. 1. The UNET architecture includes an encoder-decoder path, employing a pretrained VGG16 model for the encoder and a custom decoder. Purple arrows are used to retain details by concatenating the output of each encoder layer with its corresponding decoder layer (skip connection). (For interpretation of the references to colour in this figure legend, the reader is referred to the web version of this article.)

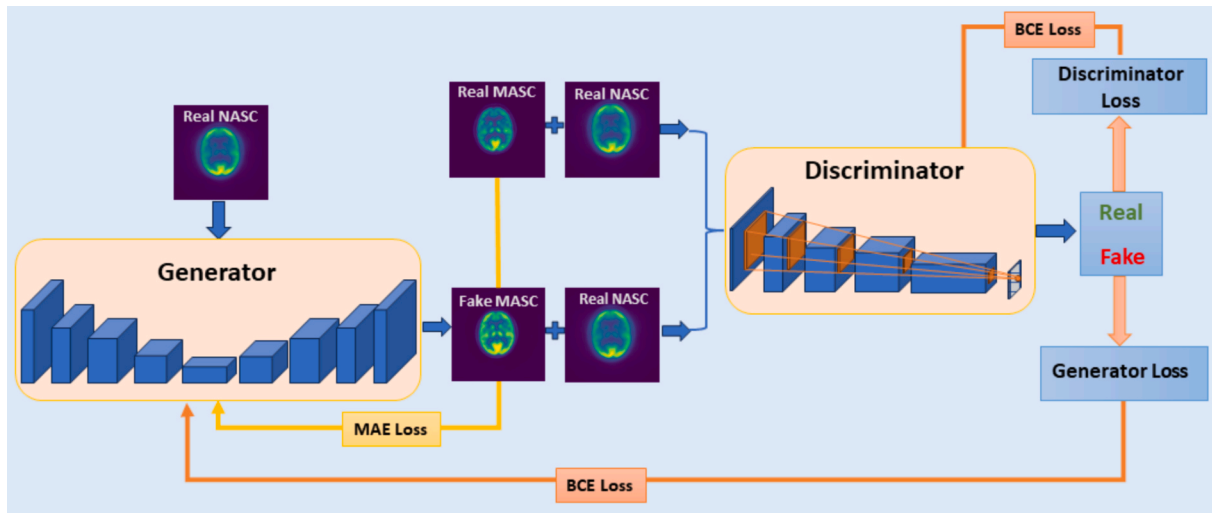


Fig. 2. The CGAN model consists of two distinct networks: Generator, which produces new images based on a given condition (initial NASC image), and Discriminator, tasked with distinguishing between real and fake images. These models are interconnected through sharing of the discriminator's loss function with the generator.

to the entire brain image, further quantitative evaluation was conducted by segmenting brain regions using HammersN30R83 atlas (Table S1) implemented in PMOD 3.8 software. This atlas includes 83 sub-regions which enable detailed region-based analysis of image quality.

Beyond conventional SUV-based evaluation, we extracted 19 radiomic feature values (RFV) from each brain sub-regions in both MASC and DL-MASC images using Pyradiomics library [54] (Table S2). These radiomic features include PET-specific uptake metrics (SUV, SUVmean, SUVmax, TLG), first-order intensity statistics (quartiles, median, energy, AUC, entropy, kurtosis), and texture features from GLCM, GLRLM, and GLSZM. These were selected to provide a compact yet comprehensive set capturing intensity distribution, heterogeneity, and spatial texture patterns, based on their frequent use and interpretability in PET radiomics literature [11]. These advanced features enabled a more detailed comparison of CGAN and UNET reconstructions, demonstrating the models' ability to preserve textural and structural characteristics beyond SUV metrics. We employed the Relative Error (RE) Eqn. (1) metric, which calculates percentage of difference between predicted and groundtruth RFV's for each patients' sub-region. Furthermore, the minimum and maximum differences for each radiomic feature among all sub-regions and the number of brain regions with significant differences in feature values were assessed among 12 test patients.

$$RE(\%) = \frac{RFV_{DL-MASC} - RFV_{MASC}}{RFV_{MASC}} \times 100\% \quad (1)$$

6. Clinical evaluation

To evaluate image quality, DL-MASC and MASC of 12 patients in test set were assessed by two nuclear medicine physicians. Scoring, scale 0–5 with 0.1 precision to allow finer discrimination (e.g. 4.8), was performed on brain images regarding image quality and lesion detectability, where 0 indicates poor quality and low diagnostic value and 5 represent excellent quality, which is assigned to groundtruth images.

7. Statistical analysis

A paired sample *t*-test was performed using R-statistics to compare radiomic features extracted from DL-MASC and MASC images across 83 brain regions. For each of the 19 radiomic features and each brain region, the differences between DL-MASC and MASC values were calculated and averaged across 12 patients in the test set. The resulting *p*-values were compared against a common level of 0.05, with *p*-values <

0.05 considered statistically significant.

8. Result

The learning curves of UNET are illustrated in Fig. S1. As mentioned previously the UNET converged after approximately 50 epochs, with the loss reaching MSE of 2.38×10^{-5} in the training set and 4.96×10^{-5} in the validation set after 1000 epochs. While the convergence is not imminent in CGAN [55,56], the best performance of CGAN model was achieved only after 637,320 steps equivalent to 60 epochs, which is demonstrated in learning curve of generator plotted based on MAE loss (Fig. S2). At the final step MAE reached 0.0039, and the discriminator loss was 0.41. The high discriminator BCE loss indicates that the model cannot distinguish between real and fake data since generator produces samples which are realistic enough to fool the discriminator.

Fig. 3-A displays slices of a PSF-reconstructed scan (NASC, DL-MASC, MASC, bias map, CT) predicted by the UNET model. The bias map illustrates the differences between DL-MASC and MASC. Fig. 3-B, presents the corresponding slices for the same patient predicted by CGAN model. Similarly, Fig. 4-A and 4-B display slices of a TOF + PSF-reconstructed scan for another patient, predicted by UNET and CGAN model, respectively. This visual comparison demonstrates the robustness of UNET and CGAN models in prediction of both types of reconstruction.

Table 1 summarizes the quantitative metrics calculation for the UNET and CGAN models, including SSIM, RMSE and PSNR, which compare MASC and DL-MASC values. As the test set consists both groups of TOF + PSF and PSF reconstruction techniques, results for each model are reported for all 12 test samples; mixed (both TOF + PSF and PSF), as well as separately for the 6 TOF + PSF and 6 PSF samples. It can be concluded that both models were successful in generating new MASC images from NASC data.

For Further assessment, region-based quantitative analysis was conducted by segmentation of MASC and DL-MASC images in the test set, based on HammersN30R83 atlas, followed by extracting 19 radiomic features for each of the regions. Differences between paired values between MASC and DL-MASC were quantified using RE metric. As shown in the RE heat maps in Figs. S3 and S4, intensity kurtosis has the highest relative error in the predictions of both models, indicating highest difference among groundtruth and prediction.

In order to demonstrate significant differences in RFVs, a heat map was plotted reporting *p*-value for 19 radiomic features in each of the 83 brain regions, based on the paired values from all 12 patients in the test

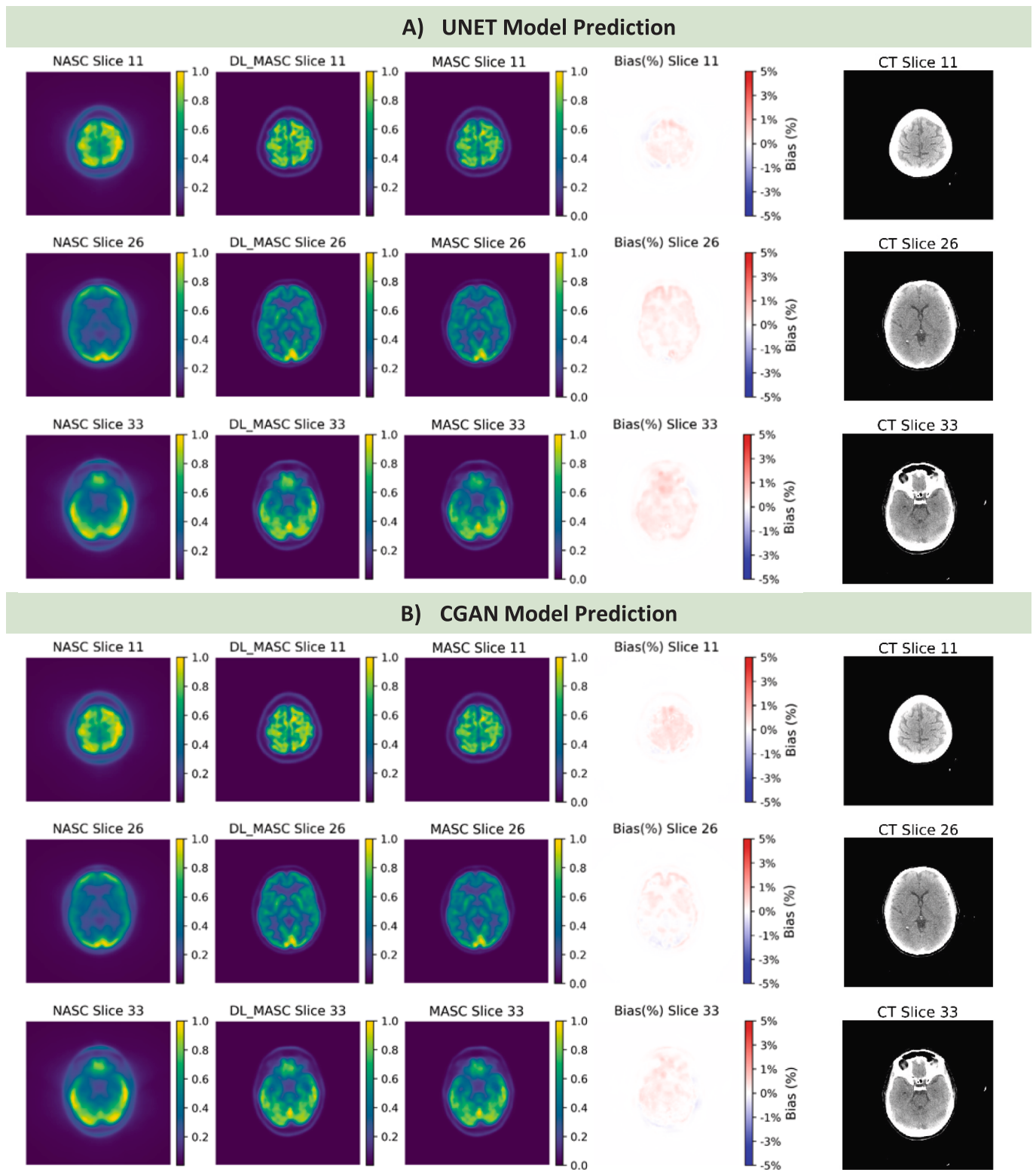


Fig. 3. NASC, DL-MASC, MASC, prediction bias image and CT of a 45-year-old female patient, reconstructed with PSF for (A) UNET model, (B) CGAN model.

set. According to the p-value heat map for the U-Net model (Fig. S5), the middle and inferior frontal gyrus in the left and right lobes exhibit the highest number of radiomic features with significant differences; 13 and 16 out of 19 features in middle frontal gyrus (FL-mid-fr-G), 8 and 9 out of 19 features in inferior frontal gyrus (FL-inf-fr-G), respectively. In contrast, as depicted in the heat map of the CGAN model (Fig. S6) the highest number of radiomic features with significant differences

appeared in the anterior cingulate gyrus (G-Cing-ant) with 10 and 13 out of 19 features, and frontal-horn with 10 and 14 out of 19 features in left and right lobes, respectively.

Fig. 5 presents box plots showing the distribution of radiomic features REs, derived from DL-MASC predictions using UNET (blue boxes) and CGAN (green boxes) models, compared to MASC for the test patients. Each box plot demonstrates the REs of a single radiomic feature

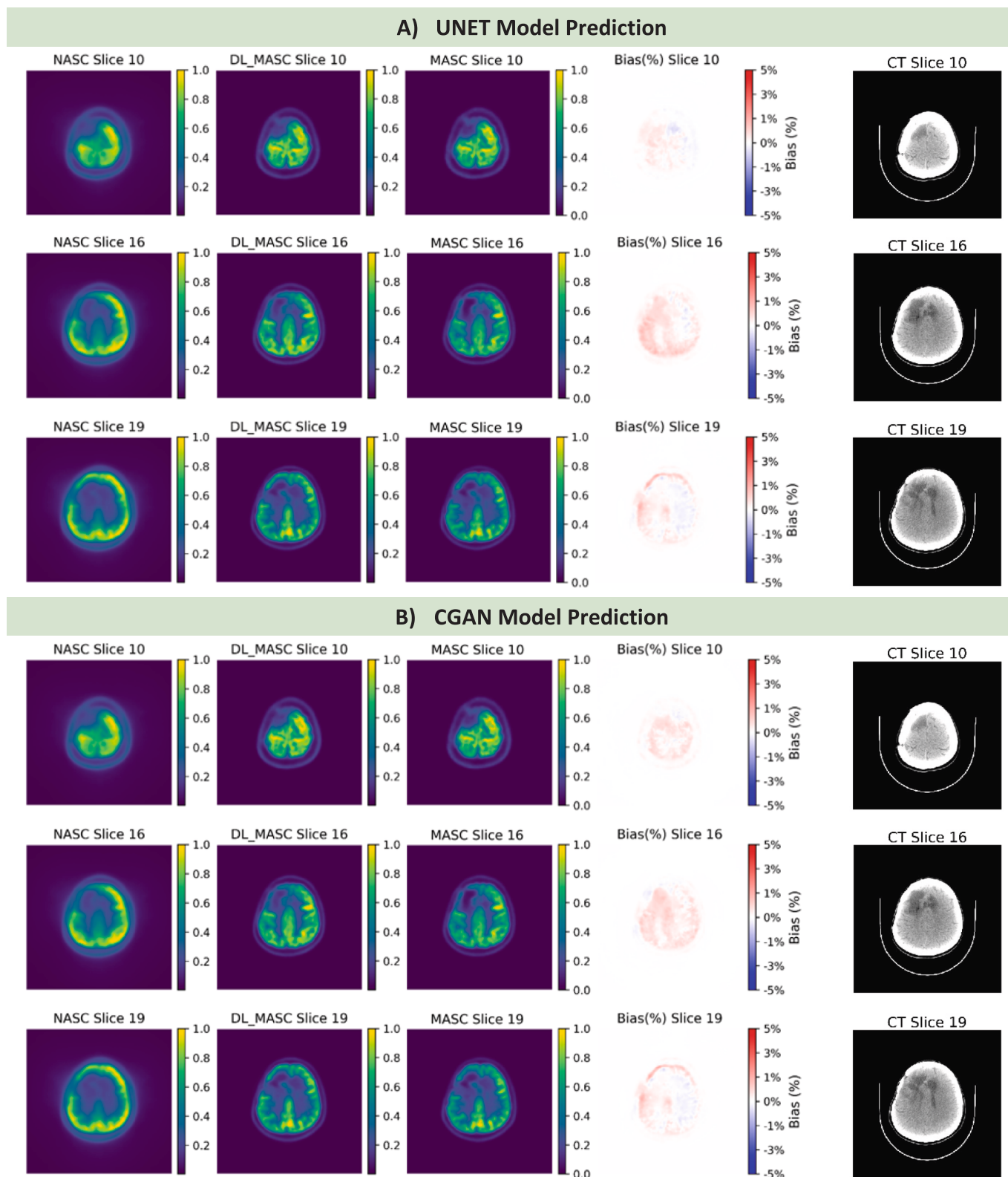


Fig. 4. NASC, DL-MASC, MASC, prediction bias images and CT of a 33-year-old male patient PET, reconstructed with TOF + PSF for (A) UNET model, (B) CGAN model.

calculated across 83 brain regions for all test patients. For reference, the red boxes represent data from Shiri et al. study [1], who extracted the same radiomic features in their study. While both UNET and CGAN predictions achieve performance comparable to Shiri’s results for most features, the CGAN model demonstrates slightly reduced variability and

greater consistency and robustness in its outcomes. These observations may reflect the effect of using transfer learning and the adversarial training used in CGAN model.

The mean, standard deviation and minimum–maximum range of radiomic features REs are presented in Table 2. Moreover, the last

Table 1

Quantitative metrics calculated on test set (Mixed), reconstructed with PSF samples and TOF + PSF samples for both UNET and CGAN models. Mixed: PSF and PSF + TOF reconstruction, RMSE: root mean squared error, PSNR: peak signal-to-noise ratio, SSIM: structural similarity index metrics.

SSIM	PSNR (dB)	RMSE (Bq/ml)	Test Set
0.996 ± 0.003	40.70 ± 3.84	327.6 ± 163.8	U-Net
Mixed			
0.997 ± 0.002	41.55 ± 3.55	294.8 ± 131.0	CGAN
Mixed			
0.997 ± 0.002	41.34 ± 3.66	294.8 ± 131.0	U-Net
PSF			
0.995 ± 0.004	39.97 ± 3.92	360.3 ± 196.5	U-Net
TOF + PSF			
0.998 ± 0.001	42.31 ± 3.66	262.08 ± 98.2	CGAN
PSF			
0.996 ± 0.002	40.67 ± 3.19	294.8 ± 131.0	CGAN
TOF + PSF			

column indicates the number of brain regions with significant differences between MASC and DL-MASC across all test patients, determined by p-values below 0.05.

The RE of SUV_{mean} was 0.95 ± 1.45 for the UNET model and 0.49 ± 0.66 for the CGAN model, with 5 and 6 regions among all test patients showing significant differences, respectively. The average RE for SUV_{max} in CGAN model predictions was -0.17 ± 1.06 , with this feature having the highest number of regions with significant differences (17regions). In the UNET model, GLCM-dissimilarity, with a mean RE of -0.86 ± 2.49 , exhibited the maximum number of regions (24regions) with a p-value below 0.05. Overall, among 1577 paired values of calculated radiomic features, 126 values in the CGAN and 156 values in the UNET predictions displayed significance differences. In conclusion, further quantitative evaluation of radiomic features between the two models indicates that the CGAN predicted fewer data points with significant

difference in comparison to the ground truth values.

Visual analysis and statistical evaluation of brain metabolism indicated the ability to detect disease using images generated by the deep learning models. While quantitative differences were observed between DL-MASC and MASC images; these discrepancies did not change clinical interpretation of physicians. Based on physicians' clinical evaluation, the U-Net model predictions achieved an average quality score of 4.84 ± 0.21 out of 5, indicating a high similarity to reference images. Similarly, the CGAN model predictions attained an average score of 4.86 ± 0.19 out of 5, demonstrating strong performance. For the two patients with significant defects, U-Net and CGAN predictions scored 4.30 ± 0.36 and 4.60 ± 0.42 out of 5, respectively for assessment of defect extent. These results reflect the high visual quality of both algorithms' outputs.

9. Discussion

In this retrospective study, we verified the possibility of using deep learning approach to perform direct ASC on ^{18}F -FDG brain PET images using two different algorithms. A UNET (Fig. 1) and a CGAN (Fig. 2) were designed and implemented to receive 2D MASC data and directly generate MASC images. While both UNET and the generator of CGAN contain convolutional networks, CGAN introduces an additional discriminator network which differentiates groundtruth from generated data. This adversarial feedback process enables the generator to improve its performance. As a result, complicated structure of CGAN is expected to enhance the prediction performance, although it comes with increasing computational demands and running time [57].

Various quantitative metrics were calculated to assess the quality of generated images, and also separately for PSF and PSF + TOF reconstructed images, to evaluate model's robustness in predicting PSF reconstruction, as well as PSF + TOF images with enhanced SNR and quality [58]. For further evaluation, segmentation of brain regions was

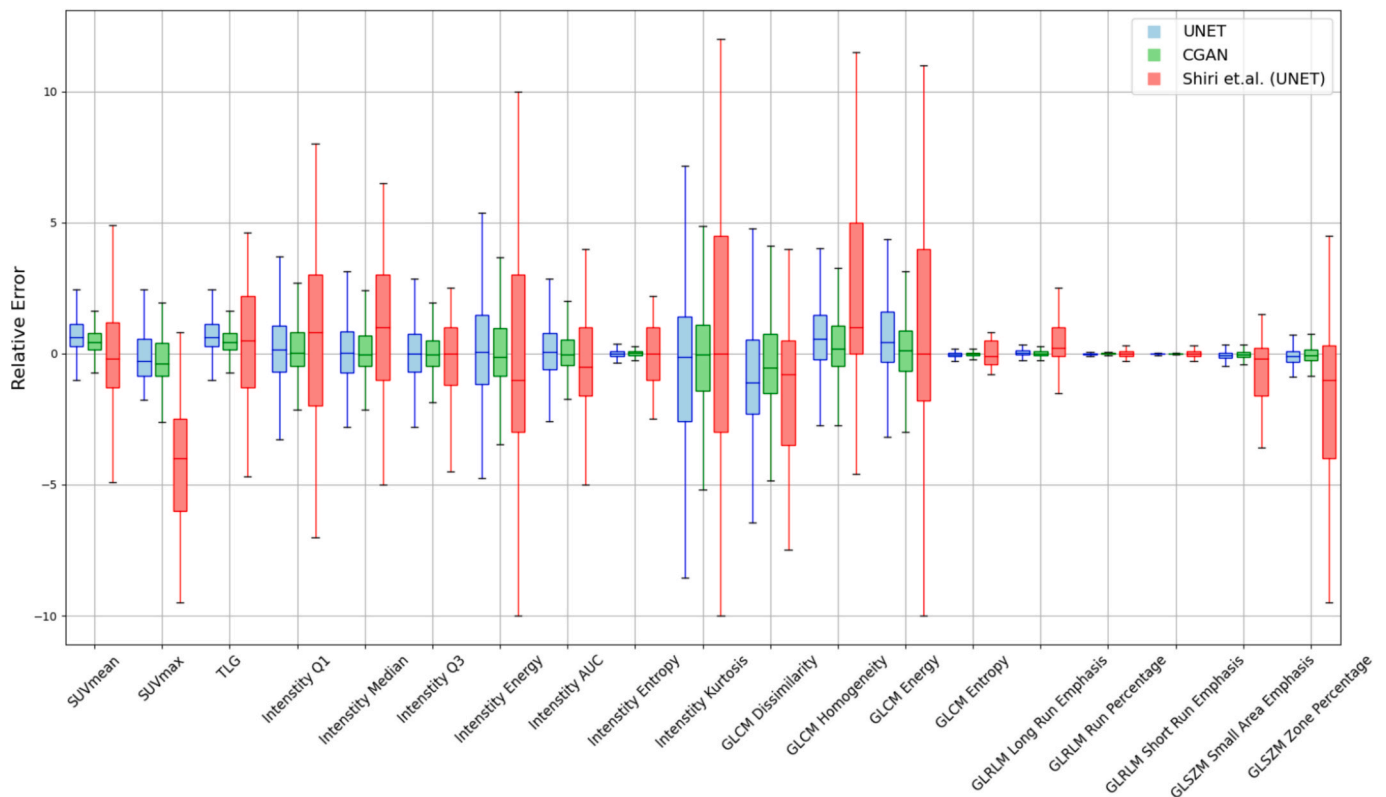


Fig. 5. Box plots of REs for 19 radiomic features, calculated across 83 brain regions in test set. Blue and green boxes represent REs among MASC and DL-MASC predicted by UNET and CGAN, respectively. Red boxes show results from Shiri et al. study (1). (For interpretation of the references to colour in this figure legend, the reader is referred to the web version of this article.)

Table 2

Summary of the mean, standard deviation (STD) and min–max range of radiomic feature’s RE in all brain regions with significance difference (p-value < 0.05). (AUC: Area Under Curve, GLCM: Gray-level co-occurrence matrix, GLRLM: Gray-level run length matrix, LRE: Long-run emphasis, RP: Run percentage, SRE: Short-run emphasis, GLZLM: Gray-level size zone matrix, SZE: Size zone emphasis, ZP: Zone percentage).

Radiomic Features	Radiomic Feature Names	Deep Learning Method	RE (Mean ± STD) All Regions	RE (min to max) All Regions	Number of Regions	
SUV	SUV _{mean}	U-Net	0.95 ± 1.45	-1.76 to 11.56	5	
	SUV _{mean}	CGAN	0.49 ± 0.66	-2.62 to 4.25	6	
	SUV _{max}	U-Net	0.06 ± 1.29	-4.49 to 4.47	9	
	SUV _{max}	CGAN	-0.17 ± 1.06	-4.81 to 4.12	17	
	TLG	U-Net	0.95 ± 1.45	-1.76 to 11.56	2	
	TLG	CGAN	0.49 ± 0.66	-2.62 to 4.25	6	
	Intensity	Q1	U-Net	0.03 ± 2.70	-9.96 to 13.82	2
		Q1	CGAN	0.28 ± 1.43	-5.15 to 10.23	4
		Median	U-Net	0.00 ± 2.16	-9.48 to 10.30	5
		Median	CGAN	0.16 ± 1.16	-3.50 to 11.31	3
Q3		U-Net	-0.05 ± 1.71	-8.99 to 12.46	7	
Q3		CGAN	0.06 ± 0.86	-4.76 to 3.72	7	
Energy		U-Net	0.15 ± 2.68	-9.84 to 13.67	6	
Energy		CGAN	0.16 ± 1.57	-4.48 to 7.34	7	
AUC		U-Net	0.00 ± 1.74	-9.06 to 11.56	5	
AUC		CGAN	0.09 ± 0.82	-2.62 to 4.25	8	
GLCM	Entropy	U-Net	-0.01 ± 0.35	-4.03 to 1.97	3	
	Entropy	CGAN	0.00 ± 0.22	-3.41 to 1.21	3	
	Kurtosis	U-Net	-0.55 ± 5.20	-13.98 to 13.03	3	
	Kurtosis	CGAN	-0.14 ± 4.30	-13.89 to 13.56	3	
	Dissimilarity	U-Net	-0.86 ± 2.49	-9.62 to 13.56	24	
	Dissimilarity	CGAN	-0.27 ± 2.46	-9.32 to 13.98	11	
	Homogeneity	U-Net	0.74 ± 2.20	-8.03 to 13.91	13	
	Homogeneity	CGAN	0.41 ± 1.99	-6.05 to 13.65	7	
	Energy	U-Net	1.00 ± 2.89	-8.54 to 15.80	8	
	Energy	CGAN	0.23 ± 2.30	-8.10 to 13.75	3	
GLRLM	Entropy	U-Net	-0.07 ± 0.40	-3.82 to 3.16	14	
	Entropy	CGAN	-0.01 ± 0.26	-2.73 to 2.26	8	
	LRE	U-Net	0.20 ± 1.01	-3.64 to 13.29	8	
	LRE	CGAN	0.00 ± 0.60	-3.46 to 9.59	3	
	RP	U-Net	0.04 ± 0.22	-2.77 to 1.29	12	
	RP	CGAN	0.00 ± 0.14	-1.48 to 1.93	6	

Table 2 (continued)

Radiomic Features	Radiomic Feature Names	Deep Learning Method	RE (Mean ± STD) All Regions	RE (min to max) All Regions	Number of Regions
SRE	SRE	U-Net	0.00 ± 0.11	-1.54 to 0.90	8
	SRE	CGAN	0.00 ± 0.08	-0.48 to 1.28	7
GLSZM	SZE	U-Net	-0.04 ± 0.54	-2.14 to 8.31	12
	SZE	CGAN	-0.03 ± 0.45	-1.87 to 7.83	9
ZP	ZP	U-Net	-0.09 ± 1.09	-7.58 to 12.63	10
	ZP	CGAN	-0.01 ± 1.00	-4.41 to 13.11	8

performed using HammersN30R83 atlas, and 19 radiomic features were extracted on each region.

Deep learning algorithms have been widely used in image-translation tasks, which applying attenuation and scatter corrections (ASC) is one of the vast fields of research. These algorithms are employed in multiple applications, such as converting MR images to CT [59], since direct attenuation correction from MR images is not available, demanding transformation of proton densities to electron densities to generate CT attenuation maps [60]. Another approach involves generating pseudo-CT images from NASC PET images [40], when challenges arise from ASC in stand-alone PET, with lack of CT and numerous difficulties in using external radionuclide, cause DL-MASC became popular in these devices [37].

Methods that rely on anatomical or structural images to generate attenuation maps for PET quantitative imaging may be affected by misalignment between anatomical information and PET data, leading to significant quantitative errors in radiotracer uptake measurements. In contrast, deep learning-based approaches, which directly perform attenuation and scatter correction in the image domain, are inherently immune to this source of error [39]. In this study we focused on comparing two models (UNET and CGAN) implemented to directly translate NASC to MASC PET images. To our knowledge, this is the first study to implement a CGAN for direct simultaneous ASC correction on ¹⁸F-FDG brain PET images and evaluation strategy with radiomic features extracted from regions in the generated images. Moreover, the use of transfer learning, incorporates in optimizing training efficiency and model convergence.

In a study published in 2019, Shiri et al. [1] developed an encoder-decoder model to attain attenuation corrected images straight from emission data. They achieved Structural Similarity Index and PSNR of 0.988 ± 0.006 and 38.70 ± 3.54 (dB) for test dataset. They also performed quantitative assessments through brain segmentation and reported a mean RE of SUV_{mean} of 0.10 ± 2.14 for all regions. In our study, simultaneous scatter and attenuation correction were applied by adding transfer learning into the UNET model and the CGAN model was further implemented. Furthermore, as demonstrated in Fig. 5, we extract the same radiomic features from brain regions as Shiri’s study; however, our models exhibit less variance and greater stability across radiomic features.

Later, Yang et al. [2] conducted research implementing DCNN as a one-step process to apply ASC on NASC brain PET images. This DCNN-method provides a potential alternative to MR-MASC. Comparing to CT-ASC as reference, the mean SUV difference was 4.0 ± 15.4 % and -4.2 ± 4.3 % for DCNN-MASC and MR-MASC, respectively. Large variance in mean difference was due to an outlier subject with tumor and by excluding this subject mean SUV for DCNN-MASC significantly improved to -0.8 ± 5.2 %. For quantitative evaluation, SUV difference between DCNN-ASC and ASC was computed for 116 automated

anatomical labels (AAL). Our proposed models achieve SUV_{mean} RE values of 0.49 ± 0.66 and 0.95 ± 1.45 for CGAN and UNET model, respectively.

In 2018, Liu et al. [8] developed a deep convolutional encoder decoder network trained by 100 FDG PET head images, to convert NAC images to pseudo-CT images. Generated CT images was compared to ground-truth with dice coefficient metric, reaching 0.80 ± 0.02 for air, 0.94 ± 0.01 for soft tissue and 0.75 ± 0.03 for bone. Further evaluation among PET attenuation corrected with pseudo-CT and ground-truth CT, demonstrates the mean error of -0.64 ± 1.99 in all regions. Our proposed models also revealed excellent performance in both attenuation and scatter corrections between NASC to MASC, with SUV_{mean} RE of 0.49 ± 0.66 for CGAN and 0.95 ± 1.45 for UNET. Moreover, in our study 83 sub-regions have been assessed separately. While the overall result was promising, in MASC images generated by UNET, inferior frontal gyrus and middle frontal gyrus have the highest number of radiomic features with significant difference compared to ground-truth (Fig. S5), and in images generated by CGAN this result acquired in frontal horn and posterior cingulate gyrus (Fig. S6).

Armanious et al. [40] purposed a CGAN include UNET-based generator and binary classifier discriminator, for independent attenuation correction of ^{18}F -FDG brain PET images. SUV difference between predicted and ground-truth images in all brain regions were below 5 % and image-based diagnosis has revealed no difference. In the current study, in addition to SUV difference, the evaluation was conducted by calculating quantitative metrics and various radiomic features. RE of 19 radiomic features in 83 brain regions has been assessed, although the most features in brain regions have the RE below 5 % which is assumed as good performance, in the results of both models Intensity Kurtosis has RE above 5 % in most brain regions (Fig. 5 and Fig. S3 and S4).

Study by Arabi et al. [41] was conducted based on Deep Learning Adversarial Semantic Structure (DL-AdvSS) for conversion of T1 weighted MR brain images to pseudo-CT. The quantitative analysis of PET images using DL approach assuming CT-based attenuation correct as reference demonstrated SUV bias less than 4 % in 63 brain regions. In this study we calculate p-value for all radiomic features in brain regions to discover datapoints with significant differences. Based on this statistical analysis, UNET demonstrated most regions (24outof83) with significant difference in GLCM-dissimilarity (-0.86 ± 2.49), while in CGAN, SUV_{max} (-0.17 ± 1.06) has the most regions with p-value below 0.05, 17 out of 83 regions (Table 2).

In our dataset, attenuation correction was performed using CT-based methods, while scatter correction employed the model-based algorithm, reflecting the standard clinical reconstruction pipeline on our PET/CT system. This choice ensured that the deep learning models were trained and evaluated on data representative of current clinical practice, aligning with our aim of developing a method that could feasibly replace both corrections simultaneously in routine workflows. While model-based scatter correction is widely used in clinics, Monte Carlo (MC) simulations are considered the gold standard for accurately modelling scatter effects. However, MC approaches require substantial computation for each individual scan, limiting their practicality for high-throughput or real-time applications. In contrast, once trained, our deep learning models can be applied rapidly at inference, offering a more scalable solution. Future work could explore the use of MC-simulated data as ground truth for training, which may further improve correction accuracy while retaining the efficiency advantages of the DL-based approach.

The performance of our proposed models can be further improved with certain enhancements in the future. Firstly, deep learning algorithms benefit from increasing the number of training and testing patients. Our study consisted of epilepsy patients, reflecting referrals to our imaging center, while attenuation and scatter corrections are physical phenomena and mostly independent of the disease type. Consequently, models should be applicable to other brain indications, and future studies including a broader range of neurological disorders will be

valuable to further validate the models and enhance generalizability of the approach. Moreover, in this study all images were acquired by ^{18}F -FDG in one center, while the multicenter studies are recommended.

10. Conclusion

In this study, we systematically compared two established deep learning architectures, UNET and CGAN, for image-to-image translation tasks, for direct simultaneous ASC on brain ^{18}F -FDG PET data. Both models demonstrated almost equal high performance in quantitative evaluations using RMSE, PSNR and SSIM parameters. These quantitative metrics were calculated separately for TOF + PSF and PSF reconstructed test samples, with both models exhibiting robust results across these groups. Radiomic feature analysis, applied here to directly compare UNET and CGAN outputs on a large paired dataset, provided complementary insight into textural and structural information beyond conventional SUV-based metrics, with CGAN showing slightly superior performance in most features. Moreover, clinical evaluations by two nuclear medicine physicians confirmed the acceptability of ASC through UNET and CGAN. While UNETs and CGANs have been used previously for PET ASC, our contribution lies in the multidimensional evaluation framework—combining quantitative, radiomic, and clinical assessments—and in training with both TOF + PSF and PSF-only data to enhance generalizability across scanner configurations. This comparable performance of DL-based ASC using UNET and CGAN, displays the potential of these methods against traditional CT-based ASC. These findings support the applicability of DL-based ASC where CT is unavailable, such as PET/MRI or stand-alone PET systems, or for dose-sensitive population and individuals requiring repeated scans.

Ethics Statement

This research complies with all relevant laws and institutional guidelines. The protocols involving human participants were approved by the Institutional Review Board (IRB) of the Tehran University of medical science under the ethic ID IR.TUMS.MEDICINE.REC.1402.188. This was a retrospective study using anonymized patient data; therefore, the requirement for informed consent was waived by the Ethics Committee.

Declaration of competing interest

The authors declare that they have no known competing financial interests or personal relationships that could have appeared to influence the work reported in this paper.

Acknowledgement

A dataset comprising 125 brain PET/CT scans were acquired at Masih Daneshvari Hospital in Shahid Beheshti University of medical sciences. Grant No. 67176, dated 19/06/2023 from Tehran University of medical science.

Appendix A. Supplementary data

Supplementary data to this article can be found online at <https://doi.org/10.1016/j.ejmp.2025.105683>.

References

- [1] Shiri I, Ghafarian P, Geramifar P, Leung KH, Yin, Ghelichoghli M. Direct attenuation correction of brain PET images using only emission data via a deep convolutional encoder-decoder (Deep-DAC). Restricted Boltzmann machine. 2019.
- [2] Yang J, Park D, Gullberg GT, Seo Y. Joint correction of attenuation and scatter in image space using deep convolutional neural networks for dedicated brain ^{18}F -FDG PET. *Phys Med Biol* 2019 Apr 4;64(7):1–22.

- [3] Wang T, Lei Y, Fu Y, Curran WJ, Liu T, Nye JA, et al. Machine Learning in Quantitative PET: A Review of Attenuation Correction and Low-count Image Reconstruction Methods. *Phys Med* 2021 Aug;1(76):294–306.
- [4] Zeraatkar N, Ay MR, Ghafarian P, Sarkar S, Geramifar P, Rahmim A. Monte Carlo-based evaluation of inter-crystal scatter and penetration in the PET subsystem of three GE Discovery PET/CT scanners. *Nucl Instrum Methods Phys Res A*. 2011;659(1):508–14.
- [5] Hemmati H, Kamali-Asl A, Ay M, Ghafarian P. Compton scatter tomography in TOF-PET. *Phys Med Biol* 2017 Sep;62(19):7641.
- [6] Shiri I, Arabi H, Geramifar P, Hajianfar G, Ghafarian P, Rahmim A, et al. Deep-JASC: joint attenuation and scatter correction in whole-body 18F-FDG PET using a deep residual network. *Eur J Nucl Med Mol Imaging* 2020 Oct 1;47(11):2533–48.
- [7] Teimourian B, Ay MR, Zafarghandi MS, Ghafarian P, Ghadiri H, Zaidi H. A novel energy mapping approach for CT-based attenuation correction in PET. *Med Phys* 2012 Apr;39(4):2078–89.
- [8] Liu F, Jang H, Kijowski R, Zhao G, Bradshaw T, Mcmillan AB. A deep learning approach for 18 F-FDG PET attenuation correction. *EJNMMI Phys* 2018;5(1):1–15.
- [9] Yang J, Sohn JH, Behr SC, Gullberg GT, Seo Y, Behr MSSC, et al. CT-less Direct Correction of Attenuation and Scatter in the Image Space Using Deep Learning for Whole-Body FDG PET : Potential Benefits and Pitfalls. *Radiol. Artif Intell* 2021. Mar 1;3(4).
- [10] Armanious K, Küstner T, Reimold M, Nikolaou K, Fougère C La, Yang B, et al. Independent brain 18 F-FDG PET attenuation correction using a deep learning approach with Generative Adversarial Networks. *Hell J Nucl Med* [Internet]. 2019; 22(3):179–86. Available from: www.nuclmed.gr.
- [11] Shiri I, Ghafarian P, Geramifar P, Leung KHY, Ghelichoghli M, Oveis M, et al. Direct attenuation correction of brain PET images using only emission data via a deep convolutional encoder-decoder (Deep-DAC). *Eur Radiol* 2019 Dec 1;29(12): 6867–79.
- [12] Hwang D, Kang SK, Kim KY, Choi H, Sung J. Comparison of deep learning – based emission – only attenuation correction methods for positron emission tomography. *Eur J Nucl Med Mol Imaging* [Internet]. 2022;1833–42. Available from: <https://doi.org/10.1007/s00259-021-05637-0>.
- [13] Shandiz MS, Rad HS, Ghafarian P, Karam MB, Akbarzadeh A, Ay MR. MR-guided attenuation map for prostate PET-MRI: an intensity and morphologic-based segmentation approach for generating a five-class attenuation map in pelvic region. *Ann Nucl Med* 2017 Jan;31(1):29–39.
- [14] Shandiz MS, Rad HS, Ghafarian P, Yaghoubi K, Ay MR. Capturing Bone Signal in MRI of Pelvis, as a Large FOV Region, Using TWIST Sequence and Generating a 5-Class Attenuation Map for Prostate PET/MRI Imaging. *Mol Imaging* 2018;17: 1536012118789314.
- [15] Khateri P, Saligheh Rad H, Jafari AH, Fathi Kazerooni A, Akbarzadeh A, Shojae Moghadam M, et al. Generation of a Four-Class Attenuation Map for MRI-Based Attenuation Correction of PET Data in the Head Area Using a Novel Combination of STE/Dixon-MRI and FCM Clustering. *Mol Imaging Biol* 2015 Dec;17(6):884–92.
- [16] Sheikhzadeh P, Sabet H, Ghadiri H, Geramifar P, Ghafarian P, Ay MR. Concept design and Monte Carlo performance evaluation of HeadphonePET: a novel brain-dedicated PET system based on partial cylindrical detectors. *J Instrum* 2018 Jul;13(07):P07008.
- [17] Arabi H, Zaidi H. Truncation compensation and metallic dental implant artefact reduction in PET/MRI attenuation correction using deep learning-based object completion. *Phys Med Biol* 2020 Sep;65(19):195002.
- [18] Blumhagen JO, Ladebeck R, Fenchel M, Scheffler K. MR-based field-of-view extension in MR/PET: B0 homogenization using gradient enhancement (HUGE). *Magn Reson Med* [Internet]. 2013 Oct 1 [cited 2025 Sep 7];70(4):1047–57. Available from: [/doi/pdf/10.1002/mrm.24555](https://doi/pdf/10.1002/mrm.24555).
- [19] Sgard B, Khalife M, Bouchut A, Fernandez B, Soret M, Giron A, et al. ZTE MR-based attenuation correction in brain FDG-PET/MR: performance in patients with cognitive impairment. *Eur Radiol* [Internet]. 2020 Mar 1 [cited 2025 Sep 11];30(3):1770–9. Available from: <https://link.springer.com/article/10.1007/s00330-019-06514-z>.
- [20] Qian P, Zheng J, Zheng Q, Liu Y, Wang T, Al Helo R, et al. Transforming UTE-mDixon MR Abdomen-Pelvis Images into CT by Jointly Leveraging Prior Knowledge and Partial Supervision. *IEEE/ACM Trans Comput Biol Bioinform* 2021 Jan 1;18(1):70–82.
- [21] Paulus DH, Quick HH, Geppert C, Fenchel M, Zhan Y, Hermosillo G, et al. Whole-Body PET/MR Imaging: Quantitative Evaluation of a Novel Model-Based MR Attenuation Correction Method Including Bone. *Journal of Nuclear Medicine* [Internet]. 2015 Jul 1 [cited 2025 Sep 7];56(7):1061–6. Available from: <https://jnm.snmjournals.org/content/56/7/1061>.
- [22] Siegel S, Dahlbom M. Implementation and Evaluation of a Calculated Attenuation Correction for PET. *IEEE Trans Nucl Sci* 1992;39(4):1117–21.
- [23] Sekine T, Buck A, Delso G, Ter Voert EEGW, Huellner M, Veit-Haibach P, et al. Evaluation of Atlas-Based Attenuation Correction for Integrated PET/MR in Human Brain: Application of a Head Atlas and Comparison to True CT-Based Attenuation Correction. *Journal of Nuclear Medicine* [Internet]. 2016 Feb 1 [cited 2025 Sep 7]; 57(2):215–20. Available from: <https://jnm.snmjournals.org/content/57/2/215>.
- [24] Krokos G, MacKewn J, Dunn J, Marsden P. A review of PET attenuation correction methods for PET-MR. *EJNMMI Phys* [Internet]. 2023 Dec 1 [cited 2025 Sep 11];10(1):1–45. Available from: <https://ejnmiphys.springeropen.com/articles/10.1186/s40658-023-00569-0>.
- [25] Mikhaylova E, Jehl M, Deidda D, Thielemans K, Dao V, Rotondi L, et al. Simulated NEMA NU2 Performance of the Ultra-Compact Clinical NeuroLF Brain PET. 2022 IEEE NSS/MIC RTSD - IEEE Nuclear Science Symposium, Medical Imaging Conference and Room Temperature Semiconductor Detector Conference. 2022.
- [26] Grogg KS, Toole T, Ouyang J, Zhu X, Normandin M, Johnson K, et al. NEMA and clinical evaluation of a novel brain PET-CT scanner HHS Public Access. *J Nucl Med* 2016;57(4):646–52.
- [27] Onishi Y, Isobe T, Ito M, Hashimoto F, Omura T, Yoshikawa E. Performance evaluation of dedicated brain PET scanner with motion correction system. *Ann Nucl Med* [Internet]. 2022 Aug 1 [cited 2025 Sep 7];36(8):746–55. Available from: <https://pubmed.ncbi.nlm.nih.gov/35698016/>.
- [28] Zaidi H, Koral KF. Scatter modelling and compensation in emission tomography. *Eur J Nucl Med Mol Imaging* 2004;31(5):761–82.
- [29] Brokowski CAM. 乳鼠心肌提取 HHS Public Access. *Physiol Behav* 2019;176(5): 139–48.
- [30] Bradshaw TJ, McMillan AB. Anatomy and Physiology of Artificial Intelligence in PET Imaging. *PET Clin*. 2021 Oct 1;16(4):471–82.
- [31] Shiri I, Leung K, Geramifar P, Ghafarian P, Oveis M, Ay MR, et al. PSFNET: ultrafast generation of PSF-modelled-like PET images using deep convolutional neural network. *J Nucl Med* 2019;60(supplement 1):1369.
- [32] Sanaat A, Arabi H, Maita I, Garibotto V, Zaidi H. Projection space implementation of deep learning-guided low-dose brain pet imaging improves performance over implementation in image space. *J Nucl Med* 2020 Sep 1;61(9):1386–96.
- [33] Ronneberger O, Fischer P, Brox T. U-Net: Convolutional Networks for Biomedical Image Segmentation; 2015 May. p. 18.
- [34] Shiri I, Vafaei Sadr A, Amini M, Salimi Y, Sanaat A, Akhavanallaf A, et al. Decentralized Distributed Multi-institutional PET Image Segmentation Using a Federated Deep Learning Framework. *Clin Nucl Med* 2022;47(7).
- [35] Häggström I, Schmidlein CR, Campanella G, Fuchs TJ. DeepPET: A deep encoder-decoder network for directly solving the PET image reconstruction inverse problem. *Med Image Anal* 2019 May;1(54):253–62.
- [36] Ledig C, Theis L, Huszar F, Caballero J, Cunningham A, Acosta A, et al. Photo-Realistic Single Image Super-Resolution Using a Generative Adversarial Network. 2016 Sep 15;.
- [37] Lee JS, Member S. A Review of Deep-Learning-Based Approaches for Attenuation Correction in Positron Emission Tomography. *IEEE Trans Radiat Plasma Med Sci* 2021 Mar 1;5(2):160–84.
- [38] Sorin V, Barash Y, Konen E, Klang E. Creating Artificial Images for Radiology Applications Using Generative Adversarial Networks (GANs) – A Systematic Review. *Acad Radiol* 2020;27(8):1175–85.
- [39] McMillan AB, Bradshaw TJ. AI-based data corrections for attenuation and scatter in PET and SPECT. 2021;16(4):543–52.
- [40] Armanious K, Küstner T, Reimold M, Nikolaou K, La FC, Yang B, et al. Independent brain 18 F-FDG PET attenuation correction using a deep learning approach with Generative Adversarial Networks. *Hell J Nucl Med* 2019;22(3):179–86.
- [41] Arabi H, Zeng G, Zheng G, Zaidi H. Novel adversarial semantic structure deep learning for MRI-guided attenuation correction in brain PET/MRI. *Eur J Nucl Med Mol Imaging* 2019;46(13):2746–59.
- [42] Gholamiankhah F, Mostafapour S, Arabi H. Deep learning-based synthetic CT generation from MR images: comparison of generative adversarial and residual neural networks. *International Journal of Radiation Research*. 2022;20(1):121–30.
- [43] Izadi S, Shiri I, F. Uribe C, Geramifar P, Zaidi H, Rahmim A, et al. Enhanced direct joint attenuation and scatter correction of whole-body PET images via context-aware deep networks. *Z Med Phys* 2024.
- [44] Mostafapour S, Gholamiankhah F, Dadgar H, Arabi H, Zaidi H. Feasibility of Deep Learning-Guided Attenuation and Scatter Correction of Whole-Body 68Ga-PSMA PET Studies in the Image Domain. *Clin Nucl Med* 2021 Aug;46(8):609–15.
- [45] Arabi H, Zaidi H. Assessment of deep learning-based PET attenuation correction frameworks in the sinogram domain. *Phys Med Biol* 2021 Jul;66(14).
- [46] Arabi H, Zaidi H. Deep learning-guided estimation of attenuation correction factors from time-of-flight PET emission data. *Med Image Anal* 2020;64:101718.
- [47] Mostafapour S, Gholamiankhah F, Maroufipour S, Momenzad M, Asadinezhad M, Zakavi SR, et al. Deep learning-guided attenuation correction in the image domain for myocardial perfusion SPECT imaging. *J Comput Des Eng* 2022 Apr 1;9(2):434–47.
- [48] Armanious K, Hepp T, Küstner T, Dittmann H, Nikolaou K, La FC, et al. Independent attenuation correction of whole body (18 F) FDG-PET using a deep learning approach with Generative Adversarial Networks. *EJNMMI Res* 2020;10(1).
- [49] Goodfellow I, Pouget-Abadie J, Mirza M, Xu B, Warde-Farley D, Ozair S, et al. Generative Adversarial Nets. In: Ghahramani Z, Welling M, Cortes C, Lawrence N, Weinberger KQ, editors. *Advances in Neural Information Processing Systems*. Curran Associates, Inc.; 2014.
- [50] Isola P, Zhu JY, Zhou T, Efros AA. Image-to-image translation with conditional adversarial networks. *Proceedings - 30th IEEE Conference on Computer Vision and Pattern Recognition*. 2017. 2017-Janua:5967–76..
- [51] Hwang D, Kang SK, Kim KY, Choi H, Sung J. Comparison of deep learning – based emission – only attenuation correction methods for positron emission tomography. *Eur J Nucl Med Mol Imaging* 2022;1833–42.
- [52] Dehno A.E, Ghafarian P., Ay M. Impact of Data Diversity Across TOF and Non-TOF PET Scans on UNET Performance for Attenuation and Scatter Corrections. In. *European Journal of Nuclear Medicine and Molecular Imaging* 2024;51: S782–S783. One New York Plaza, Suite 4600, New York, NY, United States: Springer.Elkayee.
- [53] Simonyan K, Zisserman A. Very deep convolutional networks for large-scale image recognition. 3rd International Conference on Learning Representations, ICLR 2015 - Conference Track Proceedings. 2015;1–14.
- [54] van Griethuysen JJM, Fedorov A, Parmar C, Hosny A, Aucoin N, Narayan V, et al. Computational Radiomics System to Decode the Radiographic Phenotype. *Cancer Res* 2017 Nov;77(21):e104–7.

- [55] Elaraby N, Barakat S, Rezk A. OPEN A conditional GAN – based approach for enhancing transfer learning performance in few – shot HCR tasks. *Sci Rep* [Internet]. 2022;1–18. Available from: <https://doi.org/10.1038/s41598-022-20654-1>.
- [56] Mescheder L, Geiger A, Which NS. *Training Methods for GANs do actually Converge ?* 2018.
- [57] Collazos Gonzalez J, Rincon Perez K, Barros T, Corso G, Araújo J. A Comparison of U-Net with Conditional Generative Adversarial Networks and Cycle-Consistent Adversarial Networks for real seismic data interpolation: Tupi Field. *Research, Society and Development*. 2024;13:e1613746226.
- [58] Murata T, Miwa K, Miyaji N, Wagatsuma K, Hasegawa T, Oda K, et al. Evaluation of spatial dependence of point spread function-based PET reconstruction using a traceable point-like ^{22}Na source. *EJNMMI Phys* 2016;3(1):9.
- [59] Mehranian A, Arabi H. *Vision 20 / 20 : Magnetic resonance imaging-guided attenuation correction in PET / MR. Challenges, solutions, and opportunities*. 2016;43(ii).
- [60] Zaidi H, Hasegawa B. Determination of the attenuation map in emission tomography. *J Nucl Med* 2003;44(2):291–315.